



In-situ formation of hierarchical 1D-3D hybridized carbon nanostructure supported nonnoble transition metals for efficient electrocatalysis of oxygen reaction

Jinyuan Liu^a, Hui Xu^{a,*}, Hongping Li^a, Yanhua Song^b, Jingjie Wu^c, Yongji Gong^d, Li Xu^a, Shouqi Yuan^a, Huaming Li^a, Pulickel M. Ajayan^{e,*}

^a School of the Environment and Safety Engineering, Institute for Energy Research, Jiangsu University, Zhenjiang 212013, PR China

^b School of Environmental and Chemical Engineering, Jiangsu University of Technology, Zhenjiang 212003, PR China

^c Department of Chemical and Environmental Engineering, University of Cincinnati, Cincinnati, OH, 45221, USA

^d School of Materials Science and Engineering, Bethang University, Beijing, PR China

^e Department of Materials Science and Nano Engineering, Rice University, Houston, TX, 77005, USA

ARTICLE INFO

Keywords:

Carbon nanotubes
Carbon sphere
Oxygen reduction reaction
Oxygen evolution reaction
Bi-functional electrocatalyst

ABSTRACT

Electrocatalysis of oxygen reaction is a critical step in operation of fuel cells and metal-air batteries. For the practical applications, the inexpensive non-noble metals catalysts with highly activity and stable need to be explored and utilized. Herein, a strategy for the preparation of a bi-functional rambutan shaped oxygen electrocatalyst is presented. The novel electrocatalyst is formed *in situ* with N doped carbon nanotubes grown on metal encapsulated hollow-mesoporous carbon sphere (Me@N-CNT/HMCS). The Me@N-CNT/HMCS oxygen electrocatalysts show high catalytic activities towards ORR, comparable to commercial Pt/C catalyst. The optimized performance of Fe@N-CNT/HMCS was achieved with a positive onset potential of 1.012 V and half-wave potential of 0.833 V. It is emphasized that Me@N-CNT/HMCS shows high stability and enhanced tolerance against methanol in alkaline medium. The Fe@N-CNT/HMCS electrocatalyst possessed a high OER activity with a low overpotential of 0.35 V at 10 mA cm⁻² current density. The excellent performance could be attributed to the synergistic effect involving chemical composition, high conductivity, good porosity and unique rambutan-like structure. In addition, the theoretical calculation study suggests that metallic Fe cluster can promote the O₂ adsorption strength in such chemical environment.

1. Introduction

Oxygen reduction reaction (ORR) and oxygen evolution reaction (OER) are critical to the operation of sustainable energy storage and conversion devices [1–4]. Extensive efforts have been devoted to developing catalysts to overcome the sluggish reaction kinetics [5–8]. Among all screened candidates, Pt group materials are known to be the most efficient ORR catalysts [9], while the Ir and Ru oxides perform the best performance in case of OER catalysts [10]. However, their practical applications are limited by poor durability, scarcity, and high cost. To overcome these barriers and implement large-scale application, non-noble metal electrocatalysts have rich resources and potential catalytic activity in oxygen catalysis, which are expected to replace noble metal catalysts [11,12].

In recent years, a wide range of low-cost materials, including

nanostructured carbons [13,14], non-noble transition metal oxides [15,16], carbides/nitrides and their composites [17–20] have been shown to possess moderate activity towards oxygen electrocatalysis. Carbon materials with different structures and morphology have been developed owing to their high stability and low-cost. Multi-dimensional carbon nanomaterials show different activity and stability in oxygen reactions [21–25]. For instance, the transition metal modified N doped 3D carbon sphere electrocatalysts have attracted great attention in the oxygen electrochemical studies [26–29], due to the numerous advantages including stable loading of metal nanoparticles as active materials on the surface of carbon spheres, additional catalytic sites provided by N doped hollow-mesoporous carbon sphere (denoted as: N-HMCS), high surface area and hollow-mesoporous structure that provide an expedite channel for the O₂ and electrolyte diffusion [30–35]. However, it remains an issue to further enhance oxygen catalytic

* Corresponding authors.

E-mail addresses: xh@ujs.edu.cn (H. Xu), ajayan@rice.edu (P.M. Ajayan).

<https://doi.org/10.1016/j.apcatb.2018.10.013>

Received 19 July 2018; Received in revised form 29 September 2018; Accepted 6 October 2018

Available online 09 October 2018

0926-3373/ © 2018 Elsevier B.V. All rights reserved.

activity and improve the electrical conductivity of the hollow-mesoporous carbon spheres. According to the literature, the control of structure and components of non-noble-metal electrocatalysts has been regarded as the key to improve the catalytic performance. Thus, CNTs have been used as additives to further improve conductivity and active sites of carbon sphere due to its superior electrical conductivity and high specific surface area [36–41]. The CNTs are usually introduced through simple mechanical mixing, which may easily lead to agglomeration affecting catalytic performance. The available synthesis procedures for 1D CNTs modified 3D carbon sphere usually involve multi-steps and complicate conditions [42]. It is difficult to construct hybrids with strong coupling between CNTs and carbon sphere. Therefore, the fabrication of 1D CNTs/3D carbon sphere materials with desirable porosity and high conductivity is extremely essential to achieve enhanced catalytic performance.

Herein, we demonstrate a bottom-up method to fabricate a novel hybrid rambutan-like carbon nanostructure as an active and stable bifunctional electrocatalyst for ORR and OER. The synthesis involves *in situ* formation of N doped carbon nanotubes on metal encapsulated hollow-mesoporous carbon sphere (HMCS). Due to its unique rambutan-like structure, chemical composition, rich porous structure and higher specific surface area, the hybrid material exhibited extraordinary electrocatalytic performance and stability toward ORR and OER. In case of ORR Fe@N-CNT/HMCS exhibited the onset and half-wave potential of 1.012 V and 0.833 V respectively, which is comparable performance to that of Pt/C. For OER, the Fe@N-CNT/HMCS required a low overpotential of 0.35 V for a current density of 10 mA cm⁻². In addition, the theoretical calculation study suggests that metallic Fe cluster can promote the O₂ adsorption strength in such chemical environment. The strategy presented here provides a novel and efficient approach to design bifunctional carbon-based electrocatalysts for ORR and OER.

2. Experimental section

2.1. Synthesis of metal encapsulated in nitrogen-doped carbon nanotubes wrapped hollow-mesoporous carbon spheres (Me@N-CNT/HMCS)

The SiO₂@RF spheres were prepared by a modified Stöber coating method according to the previous literature [43]. In this work, melamine, metal acetate and SiO₂@RF spheres were dissolved in methanol solution at room temperature to form a homogenous solution. The optimum mass ratio of metal acetate to melamine (which was the key to reach optimal activity) were determined through a series of experiments with different mass ratios. After stirring at room temperature, the methanol was full evaporated from the complex suspension; the dried product was ground to obtain a fine power. A subsequent one-step annealing was carried out at 800 °C for 2 h in Ar with a ramp rate of 5 °C min⁻¹ to generate the final samples. After the composites immersed in 4 M NH₄HF₂ solutions for 24 h, the SiO₂ colloidal cores were removed. The metal encapsulated in nitrogen-doped carbon nanotubes growth on hollow-mesoporous carbon sphere were prepared (denoted as: Me@N-CNT/HMCS). Typically, to synthesize Co@N-CNT/HMCS, 0.2 g cobalt acetate tetrahydrate and a certain amount of SiO₂@RF spheres were dissolved along with 0.3, 0.5, 0.7 and 1.0 g of melamine in 15 mL methanol. In this paper, we name the samples as Co@N-CNT/HMCS-X, in which X represent serial number (X = 1, 2, 3 and 4 corresponding to metal acetate: melamine = 2:3, 2:5, 2:7 and 2:10).

The preparation method of Fe@N-CNT/HMCS and Ni@N-CNT/HMCS is same as the Co@N-CNT/HMCS.

The pristine nitrogen doped carbon spheres were also prepared using similar route without the adding of metal acetate, and we name the samples as N-HMCS.

2.1.1. Synthesis of physical mixture of N-HMCS and Fe@N-CNTs

Typically, Fe@N-CNTs was synthesized by a simple pyrolysis. In

brief, 0.2 g of iron acetate tetrahydrate, 0.7 g melamine and 10 mL methanol under stirring at room temperature under completely dry. The obtained mixture was then transferred to the tube furnace and heated at 800 °C, and maintained at 800 °C for 2 h under Ar atmosphere. The resulting product was etching by 4 M NH₄HF₂ solution, and stirring overnight to remove unstable metallic nanoparticles and inactive species, resulting in the Fe@N-CNTs. Finally, N-HMCS and Fe@N-CNTs powers were finely ground together to form the physical mixture of N-HMCS and Fe@N-CNTs as a reference.

2.1.2. Synthesis of Fe-HMCS

In a typical synthesis of Fe-HMCS, 0.2 g of iron acetate tetrahydrate, 0.5 g SiO₂@RF spheres and 10 mL methanol under stirring at room temperature under completely dry. The obtained mixture was then transferred to the tube furnace and heated at 800 °C, and maintained at 800 °C for 2 h under Ar atmosphere. The resulting product was etching by 4 M NH₄HF₂ solution, and stirring overnight to remove unstable metallic nanoparticles and inactive species, resulting in the Fe-HMCS.

The preparation method of Co-HMCS is same as the Fe-HMCS.

2.2. Material characterization

The crystalline structures of Me@NCNT/HMCS were recorded by X-ray diffraction (XRD) using Shimadzu XRD-6000 with Cu K α radiation in the range of 2 θ from 10° to 80°. X-ray photoelectron spectroscopy (XPS) analysis was performed on VG MultiLab 2000 system with a monochromatic Mg-K α line source (20 kV). Brunauer-Emmett-Teller (BET) surface area was tested using N₂ adsorption and desorption at 77 K on TriStar II 3020 system. The morphologies of as-prepared catalysts were characterized using Transmission electron microscopy (TEM) (JEOL JEM-2010 microscope) at an accelerating voltage of 200 kV. The scanning electron microscopy (SEM) measurements were carried out on a JEOL JSM-7001 F energy-dispersive X-ray spectroscope (EDX). Raman spectra of as-prepared catalysts were recorded using Renishaw spectrometer with a 532 nm laser as an excitation source.

2.3. Electrochemical measurements

To fabricate the modified electrodes as follows: 4 mg as-prepared catalysts was ultrasonically dispersed in 550 μ L of water: iso-propanol = 3:1 (v/v) and 15 μ L 5% Nafion solution to form a homogeneous inks. Then 10 μ L suspension solution was drop-cast onto the polished surface of rotating disk electrode (RDE, 3 mm diameter) with an active loading amount of about 1.0 mg cm⁻². As a comparison, 10 μ L catalyst ink (1 mg mL⁻¹) of the commercial 20 wt% Pt/C is cast on the RDE surface. Electrochemical measurements were carried out at room temperature in a three electrode system connected to a CHI 760E electrochemical workstation (Chenhua Instrument), including a Pt net as counter electrode, an Ag/AgCl wire with saturated KCl solution as reference electrode and the RDE as working electrode.

2.3.1. ORR measurement

Cyclic voltammetry (CV) measurement was measured with the scanning rate of 50 mV s⁻¹ at the ambient temperature after purging O₂ or N₂ gas for 30 min. Linear sweep voltammetry (LSV) was carried on the different rotation speeds by rotating disk electrode in the O₂-saturated 0.1 M KOH solution with a scanning rate of 5 mV s⁻¹. The number of electrons (n) involved in the ORR can be performed from the rotating ring-disk electrode (RRDE, 4 mm diameter). The potential was converted to the potential versus the reversible hydrogen electrode (RHE) according to $E \text{ (vs. RHE)} = E \text{ (vs. Ag/AgCl)} + 0.197 + 0.059 \text{ pH}$.

The formation of H₂O₂ and the electron transfers number were determined from the RRDE using the equation:

$$n = \frac{4I_D}{I_D + I_R/N}$$

$$\%(H_2O_2) = 200 \times \frac{I_R/N}{I_D + I_R/N}$$

Where, I_D is the disk current, I_R is the ring current, and N is the ring correction coefficient in the RRDE experiment, which was determined to be 0.424 by the manufacturer.

2.3.2. OER measurement

The preparation procedure of as-prepared catalysts of OER measurements is different from the ORR measurement: an AC electrode was prepared by mixing iso-propanol, water and as-prepared catalysts and then spread on to 10 mm × 50 mm Ni foam with an active loading of 10 mm × 10 mm under the infrared lamp before use. The OER tests were conducted in O_2 -saturated 1 M KOH electrolyte with the scan rate of 5 mV s⁻¹ at room temperature. The reference electrode and counter electrode were same as the oxygen reduction reaction, respectively.

2.3.3. Zn-air battery measurement

A homemade Zn-air cell was employed for practical application testing of the catalysts. The Fe@N-CNT/HMCS catalyst with a loading of 1.0 mg cm⁻² coated on porous carbon paper was used to the air cathode and a polished Zn foil as the anode. 6 M KOH with 0.2 M zinc acetate mixed solution acted as electrolyte for the Zn-air battery.

3. Results and discussion

3.1. Structural and morphological characterization

The fabrication process of the rambutan-like Me@N-CNT/HMCS (Me: Fe, Co, and Ni) material has been schematically illustrated in Fig. 1a (experimental details in the Supporting Information). First, the colloidal SiO₂ spheres (Fig. S1a and S1b) were prepared via Stöber method [43]. The resorcinol-formaldehyde was used as carbon precursor wrapped on the SiO₂ surface to form the core-shell structure of SiO₂@resorcinol-formaldehyde nanospheres with a uniform shell thickness of 30–40 nm as seen in the SEM and TEM (Fig. S1c–1d). Further SiO₂@resorcinol-formaldehyde nanospheres were mixed with different kinds of metal (Fe, Co, and Ni) acetate tetrahydrate along with melamine in methanol. The uniform N doped CNTs arrays were obtained on the surface of carbon sphere by heat treatment in Ar atmosphere at 800 °C. Upon completion, an etching treatment with NH₄HF₂ was done to remove SiO₂ and unstable phases. With these simple steps, a series of Me@N-CNT/HMCS can be synthesized also demonstrating the universality of this method. From Fig. 1, all Me@N-CNT/HMCS catalysts remain well-dispersed and structurally intact even after the etching procedure. The SEM images of rambutan-like Co@N-CNT/HMCS (Fig. 1b), Ni@N-CNT/HMCS (Fig. 1c) and Fe@N-CNT/HMCS (Fig. 1d) clearly indicates that N-CNTs have grown uniformly on the surface of HMCS. The TEM of Me@N-CNT/HMCS also reveals many CNTs on the rough surface (Fig. 1e and 1g). The addition of only melamine results in N-doped hollow mesoporous carbon spheres (Fig.

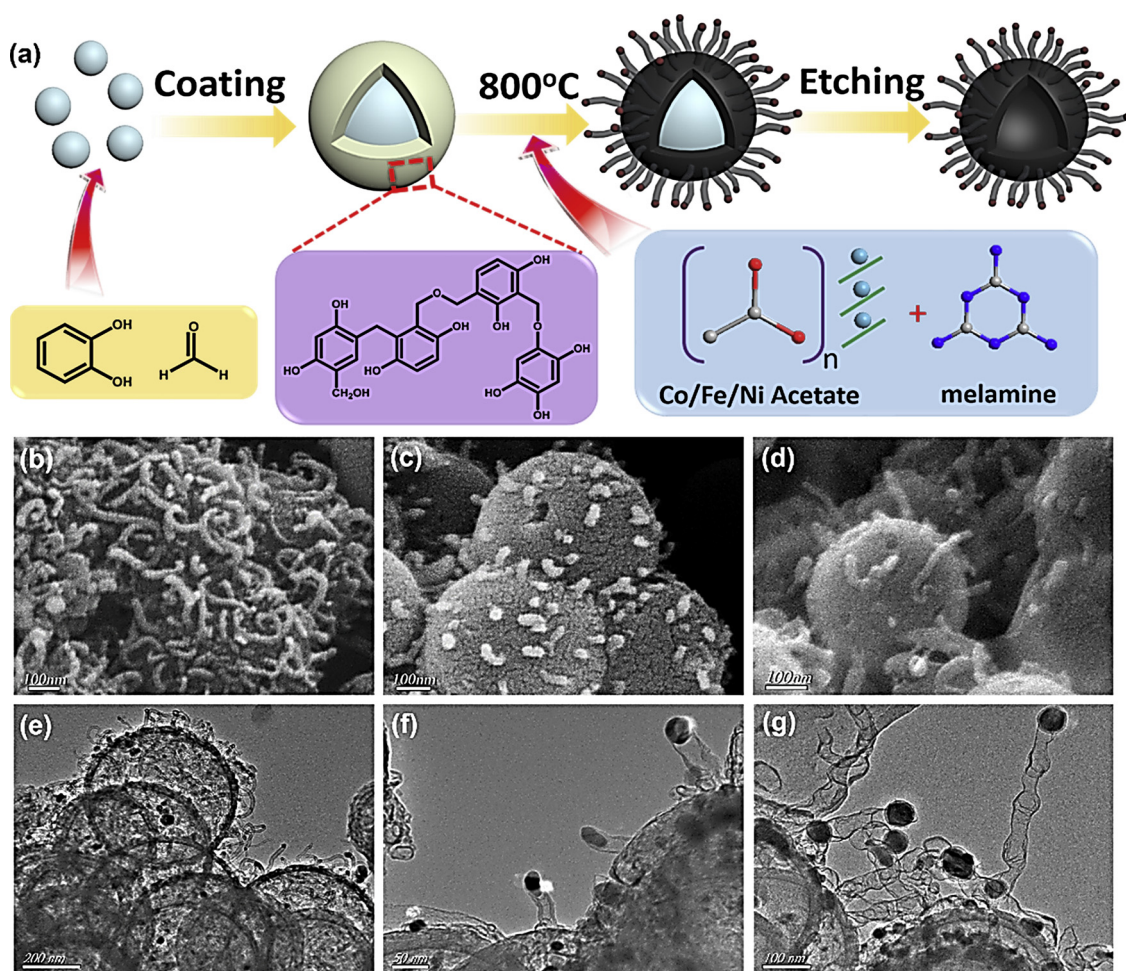


Fig. 1. (a) Schematic illustration for the synthesis process of Me@N-CNT/HMCS catalysts. The SEM images of the Co@N-CNT/HMCS (b), Ni@N-CNT/HMCS (c) and Fe@N-CNT/HMCS (d) catalysts. The TEM images of the Co@N-CNT/HMCS (e), Ni@N-CNT/HMCS (f) and Fe@N-CNT/HMCS (g) catalysts.

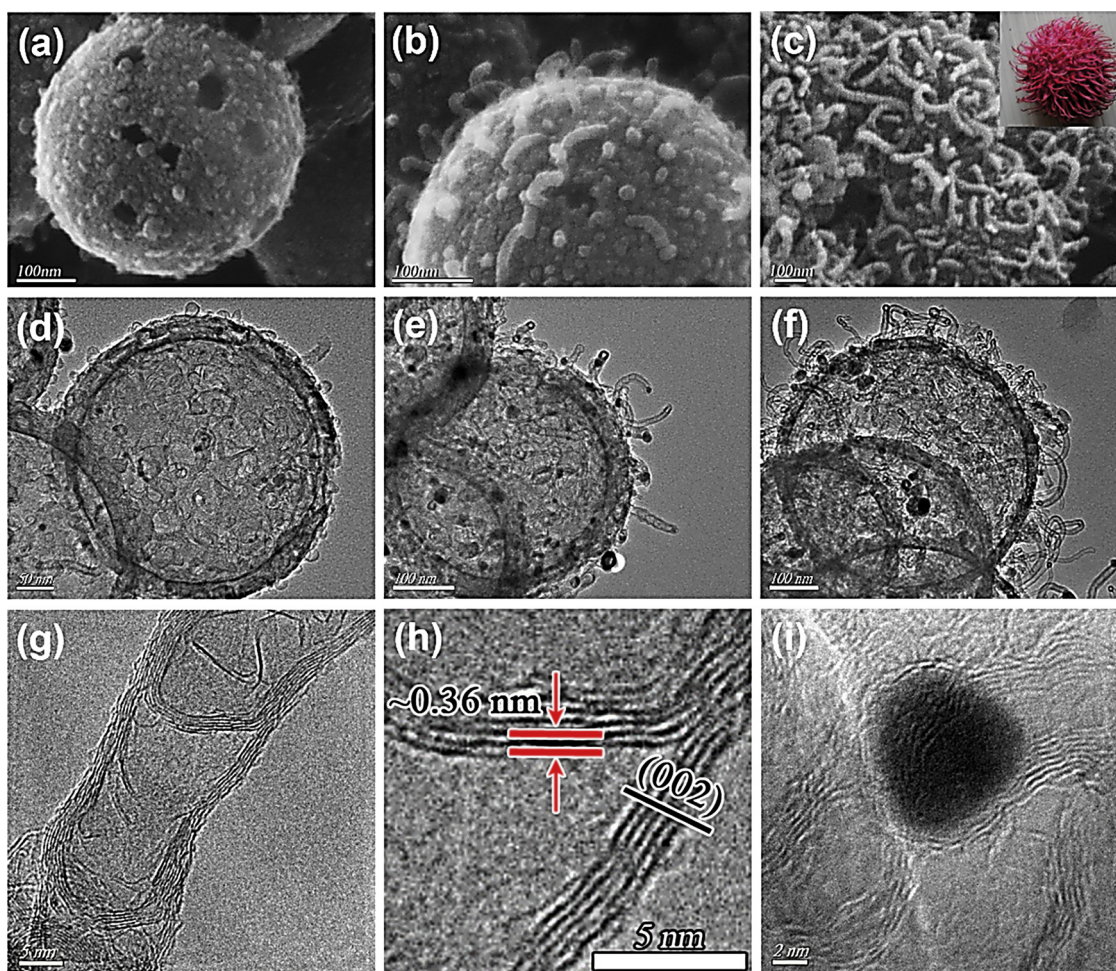


Fig. 2. The SEM images of Co@N-CNT/HMCS catalyst with different mass ratios of Co: melamine = 2:3 (a), Co: melamine = 2:5 (b) and Co: melamine = 2:7 (c); The TEM images of Co@N-CNT/HMCS catalyst with different mass ratios of Co: melamine = 2:3 (d), Co: melamine = 2:5 (e) and Co: melamine = 2:7 (f). The HRTEM image of a NCNT on Co@N-CNT/HMCS (Co: melamine = 2:7) catalyst (g) and the enlarged HRTEM images (h–i).

S1e–1f), whereas only metal precursor results in the metal-doped hollow mesoporous carbon spheres (Fig. S2) under the same calcining conditions.

The formation of the rambutan-like Me@N-CNT/HMCS electrocatalysts requires both melamine and metal in a specific mass ratio. If an alternative to melamine was used, only N-HMCS structure was obtained, which suggests that melamine serves as a potential source of C and N for the formation of rambutan shaped carbon materials [44–46]. In addition, without the presence of HMCS as support, the preparation of uniformly disperse CNTs is very difficult (Fig. S3a). It is worth mentioning that the length and density of Me@N-CNTs can be well controlled by tuning the mass ratios of metal and melamine precursor. Specifically, when the mass ratio of cobalt acetate tetrahydrate and melamine ($m_{\text{Co}} : m_{\text{melamine}}$) precursor was 2:3, the tiny N-CNTs appear on the surface of carbon spheres (Fig. 2a and d), denoted as Co@N-CNT/HMCS (2:3). With the decrease in this mass ratio to 2:5, longer N-CNTs were seen on the surface of carbon sphere denoted as Co@N-CNT/HMCS (2:5) (Fig. 2b and e). As the melamine content was further increased with $m_{\text{Co}} : m_{\text{melamine}} = 2:7$, denoted as Co@N-CNT/HMCS (2:7) (abbreviation for Co@N-CNT/HMCS), the entire surface of carbon sphere became covered with denser and longer N-CNTs clusters (length ~ 200 nm) (Fig. 2c and f). Further enhance the $m_{\text{Co}} : m_{\text{melamine}}$ to 2:10, resulted in agglomeration which eventually leads to a decrease of the hybrid performance (Fig. S3b). Notably, the above results indicate that optimal ratio of metal and melamine is needed for efficient synthesis of Me@N-CNT/HMCS. The TEM image of CNTs at the endpoints in Fig. 2f,

which reveals the tip growth mechanism with cobalt encapsulated inside the nanotubes. As established in previous research [47], typical bamboo-like “joints” represent a typical morphological feature of N-doped CNTs synthesized in this work (Fig. 2g). A high-resolution (HRTEM) image shown in Fig. 2h indicates that the outer diameter of multi-walled N-CNTs was about 2–3 nm while the encapsulated metal catalyst nanoparticle size was about 10 nm. The lattice fringes with an interlayer distance of ~ 0.36 nm correspond to the graphitic (002) plane (Fig. 2h) [48]. The measured (002) d-spacing, ranging from 0.34–0.36 nm, may facilitate incorporation of N atoms into the graphitic structure thereby enhancing the number of active sites [49]. The amount of Co atoms in Co@N-CNT/HMCS was estimated to be 0.63 at %, according to the XPS result (Table S1). The acid treatment removes unstable metallic nanoparticles but leaves metal nanoparticles encapsulated inside the tip of N-CNTs (Fig. 2i). A similar tuning of metal/melamine mass ratios was done for Fe@N-CNT/HMCS and Ni@N-CNT/HMCS (Fig. S4). The optimized mass ratio of metal/melamine precursor was found to be 2:7 for all the Me@N-CNT/HMCS systems. Finally, this approach offers a versatile novel strategy for the controlled design and synthesis of carbon-based nanomaterials with a potential for scale up.

The crystalline nature of prepared carbon material was characterized by powder X-ray diffraction (XRD) in Fig. 3a. The diffraction peaks of N-HMCS and HMCS around 24.1° was assigned to (002) plane of carbon (Fig. S5a). For Me@N-CNT/HMCS catalysts, the (002) plane carbon diffraction peaks around 26.0° became more steeper and shifted positively, indicating the increase of graphitization degrees [50]. The

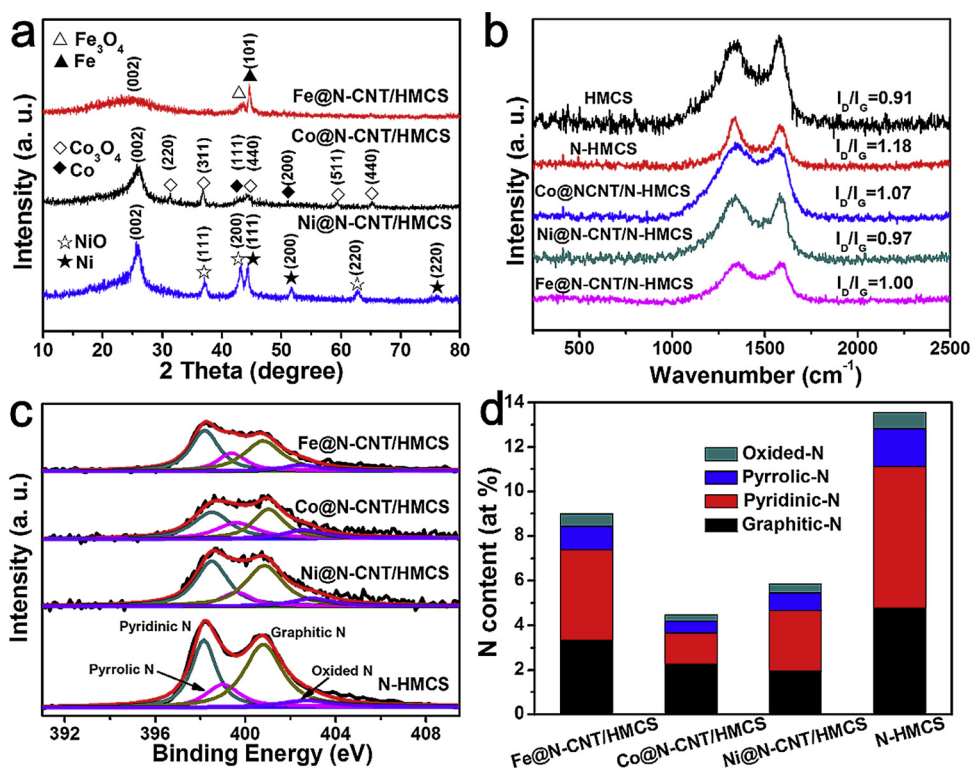


Fig. 3. XRD survey of the Me@N-CNT/HMCS catalysts (a). Raman spectra of the Me@N-CNT/HMCS catalysts (b). The high resolution N 1s XPS spectrum for the resultant Fe@N-CNT/HMCS, Co@N-CNT/HMCS, Ni@N-CNT/HMCS and N-HMCS catalyst (c). The graphitic-N, pyridinic-N, pyrrolic-N and oxidized-N content obtained from XPS measurement (d).

sharp diffraction peaks at around 44.4° , 51.8° and 76.1° match well with the (111), (200), and (220) reflections of metallic cobalt, respectively, according to JCPDS Card No. 04-0850. In addition, the diffraction peaks of metal oxides (Co_3O_4) were observed according to JCPDS Card No. 43-1049, indicating the presence of Co_3O_4 . The spectrum for Co@N-CNT/HMCS/ SiO_2 was also taken before removing the template (Fig. S5b). The intensity of Co and Co_3O_4 peaks for the Co@N-CNT/HMCS significantly decreased after the washing with NH_4HF_2 (Fig. 3a), indicating that some of the inactive species and unstable exposed particles have been removed. Furthermore, the Fe@N-CNT/HMCS (Ni@N-CNT/HMCS) materials consisting of Fe and Fe_3O_4 (Ni and NiO) peaks were also detected using XRD after the NH_4HF_2 wash. The graphitization degree of these carbon materials was also explored by Raman spectra (Fig. 3b). The characteristic D (1350 cm^{-1}) and G (1590 cm^{-1}) bands are related to the disordered or defect carbon and graphitic sp^2 -carbon, respectively. Compared to the N-HMCS sample, the decreased I_D/I_G intensity ratio of the Me@N-CNT/HMCS indicates that growth of Me@N-CNTs can facilitate improvement in the graphitization degree of the N-HMCS [51].

The surface composition of catalysts was examined by XPS measurement, which provides insightful chemical and structural information. All catalysts show the existence of C, N, and O at a comparable level (Fig. S6a). The high-resolution Co 2p XPS for Co@N-CNT/HMCS catalyst exhibits three types of Co species: metallic Co, Co(III) and Co(II) assigned to 778.4 V, 779.6 V and 781.6 V, respectively (Fig. S6c). The high-resolution Fe 2p and Ni 2p spectra of Fe@N-CNT/HMCS and Ni@N-CNT/HMCS catalyst also agree with the XRD results which indicated the presence of metallic Fe, Ni and Fe_3O_4 and NiO (Fig. S6b and S6d). The high-resolution C 1s spectrum shows two signals at $\sim 284.7\text{ eV}$ and $\sim 285.6\text{ eV}$, corresponding to the C–C, C=N, and C=O, respectively (Fig. S7). It has been reported that the C=O group on the surface of carbon material acts as the real active site for OER [52]. Nitrogen-doping has been recognized as one of the most effective strategies to create active sites in carbon-based materials [53]. The deconvolution of N 1s spectrum shows the presence of four types of nitrogen species, which can be attributed to pyridinic-N ($398.3 \pm 0.2\text{ eV}$), pyrrolic-N ($399.4 \pm 0.2\text{ eV}$), graphitic-N

($401.1 \pm 0.2\text{ eV}$) and oxidised-N ($403.8 \pm 0.2\text{ eV}$) in Me@N-CNT/HMCS catalyst (Fig. 3c). The total atomic N content of N-HMCS, Fe@N-CNT/HMCS, Co@N-CNT/HMCS and Ni@N-CNT/HMCS was 13.55 at %, 8.98 at %, 4.45 at % and 5.91 at %, respectively (Fig. 3d, Table S1 and S2). The highest pyridinic N content (4.04 at %) was seen in Fe@N-CNT/HMCS among all the Me@N-CNT/HMCS electrocatalysts. The pyridinic-N content for Co@N-CNT/HMCS and Ni@N-CNT/HMCS is 1.39 and 2.71 at%, respectively. Notably, the pyridinic-N species have been recognized as active sites of ORR in considerable studies [54].

The surface area and porosity of the Fe@N-CNT/HMCS, Co@N-CNT/HMCS and Ni@N-CNT/HMCS catalysts (Fig. S8) exhibit type-IV isotherm with a comparable high surface area of 510.37, 357.83 and $356.83\text{ m}^2\text{ g}^{-1}$, respectively. The distinct hysteresis loop in the large range of ca. 0.4–1.0 P/P₀, which indicates the presence of mesoporous structure (Fig. S8). The pore size distribution is shown in the inset of Fig. S8, the result reveals that the average pores diameter is 3.823, 3.825 and 3.576 nm for Fe@N-CNT/HMCS, Co@N-CNT/HMCS, and Ni@N-CNT/HMCS catalyst, respectively. It also indicates that numerous mesopores were generated during the high-temperature pyrolysis. Due to the typical structure of Me@N-CNT/HMCS surface, its surface area was higher than that of the HMCS and N-HMCS (Table S3).

3.2. Oxygen reduction reaction

To assess ORR performance of different metal-modified rambutan-shaped Me@N-CNT/HMCS samples, the cyclic voltammetry (CV) and linear sweep voltammogram (LSV) measurements were performed on a rotating disk electrode (RDE) in 0.1 M KOH electrolyte. The CV curves of Fe@N-CNT/HMCS, Co@N-CNT/HMCS and Ni@N-CNT/HMCS materials display obvious electrochemical oxygen reduction peak at ~ 0.784 , ~ 0.740 , and $\sim 0.697\text{ V}$, respectively, in the O_2 -saturated electrolyte (Fig. S9), while there is no reduction peak in the N_2 -saturated electrolyte. This demonstrated that the ORR activity attributed to the reduction of O_2 . The LSV measurements of Me@N-CNT/HMCS at different rotation rates were conducted with RDE instrument, revealing an ever-increasing current density attributed to shorter diffusion distance at higher speeds in Fig. S11. Based on the LSV measurements

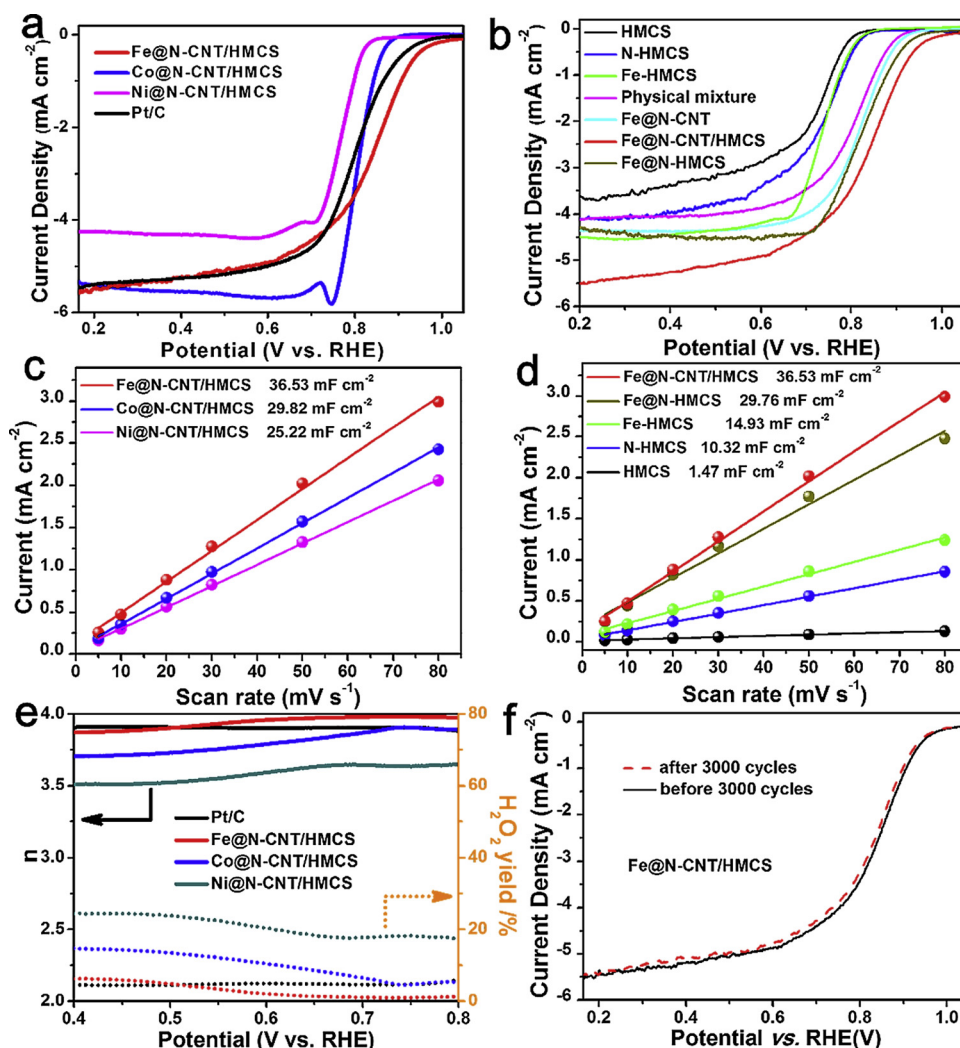


Fig. 4. Disk currents of all Me@N-CNT/HMCS (Me = Fe, Co and Ni) obtained from RDE measurements in O₂-saturated 0.1 M KOH at a sweep rate 5 mV s⁻¹, 1600 rpm compared with Pt/C (a). The polarization curves of HMCS, N-HMCS, Fe-HMCS, Fe@N-CNT, physical mixture N-HMCS and Fe@N-CNT (mass ratio = 1:1) and Fe@N-CNT/HMCS obtained from RDE measurements in O₂-saturated 0.1 M KOH at a sweep rate 5 mV s⁻¹, 1600 rpm (b). The double layer capacity (C_{dl}) of Fe@N-CNT/HMCS, Co@N-CNT/HMCS and Ni@N-CNT/HMCS catalyst (c). The C_{dl} of Fe@N-CNT/HMCS, Fe@N-HMCS, Fe-HMCS, N-HMCS and HMCS catalyst (d). The electron transfer number (n) per oxygen and percentage of H₂O₂ formation for the Me@N-CNT/HMCS (Me = Fe, Co and Ni) and Pt/C calculated from RRDE measurement in O₂-saturated 0.1 M KOH at a scan rate of 5 mV s⁻¹, rotation rate = 1600 rpm (e). The ORR polarization curves of Fe@N-CNT/HMCS before and after 3000 cycles (f).

using the onset potential (E_0) and half-wave potential ($E_{1/2}$) as the criteria, the Fe@N-CNT/HMCS ($E_0 = 1.012$ V, $E_{1/2} = 0.833$ V) exhibits catalytic activity far superior to Ni@N-CNT/HMCS ($E_0 = 0.848$ V, $E_{1/2} = 0.770$ V), and also slightly higher than Co@N-CNT/HMCS ($E_0 = 0.901$ V, $E_{1/2} = 0.807$ V) in (Fig. 4a, Table S4). Notably, the Fe@N-CNT/HMCS displays comparable performance to Pt/C ($E_0 = 1.00$ V, $E_{1/2} = 0.835$ V). Several control samples were tested in order to reveal the origin of activity for Fe@N-CNT/HMCS. The ORR activity of Fe-HMCS ($E_0 = 0.847$ V, $E_{1/2} = 0.741$ V) and N-HMCS ($E_0 = 0.847$ V, $E_{1/2} = 0.730$ V) obviously outperforms HMCS ($E_0 = 0.847$ V, $E_{1/2} = 0.722$ V), making it clear that Fe-loading or N-doping contribute to the ORR performance to some extent (Fig. 4b). In particular, the Fe@N-CNT ($E_0 = 0.955$ V, $E_{1/2} = 0.819$ V) and Fe@N-HMCS ($E_0 = 0.981$ V, $E_{1/2} = 0.829$ V) exhibit better performance than N-HMCS and Fe-HMCS, this indicates that the synergistic effect between iron (loaded Fe) and nitrogen (doped N) play an important role in the ORR process. Meanwhile, the Fe@N-CNT possesses comparative advantage compared with Fe@N-HMCS due to the morphology effect. It is worth noting that the optimized Fe@N-CNT/HMCS exhibit higher activity than Fe@N-CNTs or N-HMCS alone or the physical mixture of Fe@N-CNTs and N-HMCS (mass ratio = 1:1), revealing the synergistic effect between Fe@N-CNT and N-HMCS. The above results confirm that *in-situ* Fe@N-CNT as main active sites boosting ORR. To explore possible reasons for the enhanced catalytic activity, we have measured C_{dl} of the electrocatalysts to evaluate their electrochemical active surface area (ECSA). Specifically, the CV curves in a small potential range of 1.064–1.364 V without any

redox reaction at various scan rates from 5 to 80 mV s⁻¹ (Fig. S12) were carried to calculate C_{dl}. The C_{dl} of all sample was calculated by plotting $j = (j_a - j_c)/2$ at 1.214 V against the CV scan rates, as shown in Fig. 4c-d. As expected, the Fe@N-CNT/HMCS (36.53 mF cm⁻²) exhibit the largest C_{dl} values compare with Co@N-CNT/HMCS (29.82 mF cm⁻²) and Ni@N-CNT/HMCS (25.22 mF cm⁻²), implying that the great promotion of Fe in comparison to Co and Ni (Fig. 4c). Besides, the C_{dl} of Fe@N-CNT/HMCS, Fe@N-HMCS, Fe-HMCS, N-HMCS and HMCS are calculated to be 36.53, 29.76, 14.93, 10.32 and 1.47 mF cm⁻², respectively. The result illustrates that the introduction of both iron and nitrogen will further increase the ECSA of Fe@N-CNT/HMCS and Fe@N-HMCS than that of Fe doped, N doped or no doped materials. The special 1D CNT-3D HMCS structure of Fe@N-CNT/HMCS is more advantageous to the exposure of active sites. So, the Fe@N-CNT/HMCS possesses a larger ECSA than that of Fe@N-HMCS. The larger ECSA is conducive to the ORR, which can explain that the best electrocatalytic ORR activity of Fe@N-CNT/HMCS is relevant to the largest ECSA at the solid-liquid interface [55]. The H₂O₂ yield and electron transfer number (n) which are useful to identify oxygen reduction products and ORR reaction pathway were extracted from the rotating ring-disk electrode (RRDE) measurements (Fig. 4e). The H₂O₂ yields of the Fe@N-CNT/HMCS is similar to the Pt/C and lower than 5.52%, which is far below the Co@N-CNT/HMCS and Ni@N-CNT/HMCS materials. The n value of Fe@N-CNT/HMCS is 3.87–3.99, which is close to that of the Pt/C catalyst and is higher than that of Co@N-CNT/HMCS (3.70–3.90) and Ni@N-CNT/HMCS (3.51–3.64). The highest n and lowest peroxide yield of

Fe@N-CNT/HMCS suggest the most efficient 4-e ORR kinetics. Equally important, the Me@N-CNT/HMCS catalysts showed high stability for ORR in alkaline solution. No negative shift of ORR polarization curve was observed after 3000 cycles CV tests (Fig. 4f, S13a and S13c). No visible change in robust 1D-3D rambutan-like nanostructure was observed for Fe@N-CNT/HMCS electrocatalyst after 3000 continuous potential cycles as confirmed by TEM analysis (Fig. S14). In contrast, the commercial Pt/C catalyst had a 40 mV negative shift in the half-wave potential under the same conditions (Fig. S15a). In addition, there is no oxidation peak of methanol in the CV for Me@N-CNT/HMCS (Fig. S13b, S13d and S13e), while the commercial Pt/C exhibits typical inverse methanol oxidation peaks in the CV (Fig. S15b). This demonstrates that the Me@N-CNT/HMCS possesses a stronger tolerance against crossover effect than commercial Pt/C catalyst. We also compared Me@N-CNT/HMCS with previously reported highly efficient ORR electrocatalysts. The excellent catalytic activity of Fe@N-CNT/HMCS is comparable to other reported carbon-based ORR catalysts in terms of onset potential, half-wave potential, and limited current density (Table S5).

3.3. Oxygen evolution reaction

Then, the oxygen evolution reaction (OER) performance of Me@N-CNT/HMCS was investigated in 1 M KOH electrolyte (Fig. 5a). In Fig. S16, the Fe@N-CNT/HMCS demonstrates an overpotential of 0.34 V at the current density of 10 mA cm^{-2} (denoted as $\eta_{10} = 0.34 \text{ V}$), which is smaller than that of Co@N-CNT/HMCS ($\eta_{10} = 0.36 \text{ V}$) and Ni@N-CNT/HMCS ($\eta_{10} = 0.38 \text{ V}$). Noticeably, Fe@N-CNT/HMCS shows a slightly lower potential than those of Fe@N-CNT ($\eta_{10} = 0.36 \text{ V}$), N-HMCS ($\eta_{10} = 0.42 \text{ V}$) and physical mixing (Fe@N-CNT and N-HMCS) ($\eta_{10} = 0.37 \text{ V}$) (Table S6). In addition, the comparison results imply the synergistic effect between Fe@N-CNT and N-HMCS enhance the electrocatalytic activity over single Fe@N-CNT or N-HMCS. The results confirm that the synergetic effect arising from the interactions between Fe@N-CNT and N-HMCS. The formation of oxygen bubbles could be visually observed on the Fe@N-CNT/HMCS coated Ni foam (Fig. S17). Fig. 5b gives the overpotentials of catalysts at different current

densities. Both $\eta_{10} = 0.34 \text{ V}$ and $\eta_{30} = 0.40 \text{ V}$ for Fe@N-CNT/HMCS catalyst are much lower than those of the other samples. We also compared Fe@N-CNT/HMCS with reported OER electrocatalysts as summarized in Table S7. It's worth noting that rambutan-like Fe@N-CNT/HMCS catalyst afforded a lower overpotential at current density of 10 mA cm^{-2} comparable to those of non-precious metal electrocatalysts. For example, $\text{Mn}_3\text{O}_4/\text{CoSe}_2$ ($\eta_{10} = 0.45 \text{ V}$, in 0.1 M KOH) [56], N-graphene/CNT [57], Co-CoO/N-rGO ($\eta_{10} = 0.39 \text{ V}$, in 1 M KOH) and Ni-CoO/N-rGO ($\eta_{10} = 0.24 \text{ V}$, in 1 M KOH) [58]. Moreover, many other electrocatalysts are superior to rambutan-like Fe@N-CNT/HMCS catalyst, for instance, the $\text{Co}_3\text{O}_4/\text{N-graphene}$ ($\eta_{10} = 0.31 \text{ V}$, in 1.0 M KOH) [59] and Fe-CoOOH/graphene ($\eta_{10} = 0.33 \text{ V}$, in 1.0 M KOH) [60]. These hybrids may be some of the most promising alternatives to noble-metal catalysts, but there is still a large potential for development.

The OER kinetics were further investigated by extracting Tafel slopes. In Fig. 5c, the Tafel slopes were calculated to be 76, 88, 117 and 92 mV dec^{-1} , respectively, for Fe@N-CNT/HMCS, Fe@N-CNT, N-HMCS, and physical mixture sample (Fe@N-CNT and N-HMCS). The smallest Tafel slope for Fe@N-CNT/HMCS suggests the most favorable kinetics for OER. Fig. 5d displays the Nyquist plots of these electrodes by measuring electrochemical impedance spectroscopy (EIS). The Fe@N-CNT exhibits a smaller semi-circle compared to the N-HMCS and Fe-HMCS. This result indicated that the introduction of N-CNT as electron-bridge allows for more efficient charge transfer. For Fe@N-CNT/HMCS, the charge-transfer resistance is further reduced as the 3D hollow-mesoporous carbon architecture with a large surface area overcomes the limitations of 1D carbon nanotubes agglomeration. This typical structure made active sites exposed, and then accelerated electrons migration.

3.4. Zn-air battery performance

Considering the high bi-functional ORR/OER catalytic activity of Fe@N-CNT/HMCS, we further investigate its practical application about fabricated a Zn-air battery contains Fe@N-CNT/HMCS as the cathode catalyst and zinc foil as anode with 6 M KOH and 0.2 M $\text{Zn}(\text{Ac})_2$

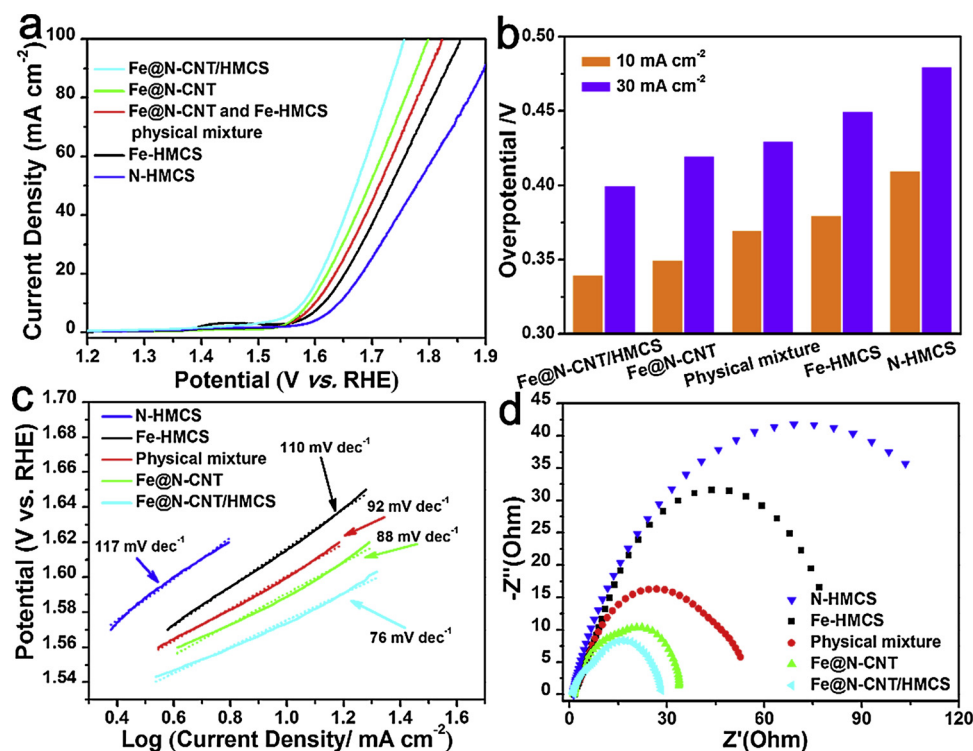


Fig. 5. Polarization curves of the N-HMCS, Fe-HMCS, Fe@N-CNT, physical mixture (N-HMCS and Fe@N-CNT) and Fe@N-CNT/HMCS electrocatalysts for OER in 1.0 M KOH electrolyte (a). The overpotential required of N-HMCS, Fe-HMCS, Fe@N-CNT, physical mixture (N-HMCS and Fe@N-CNT) and Fe@N-CNT/HMCS for achieving current of 10 and 30 mA cm^{-2} (b). Tafel plots of N-HMCS, Fe-HMCS, Fe@N-CNT, physical mixture (N-HMCS and Fe@N-CNT) and Me@N-CNT/HMCS electrocatalysts (c). Nyquist plots of N-HMCS, Fe-HMCS, Fe@N-CNT, physical mixture (N-HMCS and Fe@N-CNT) and Fe@N-CNT/HMCS (d).

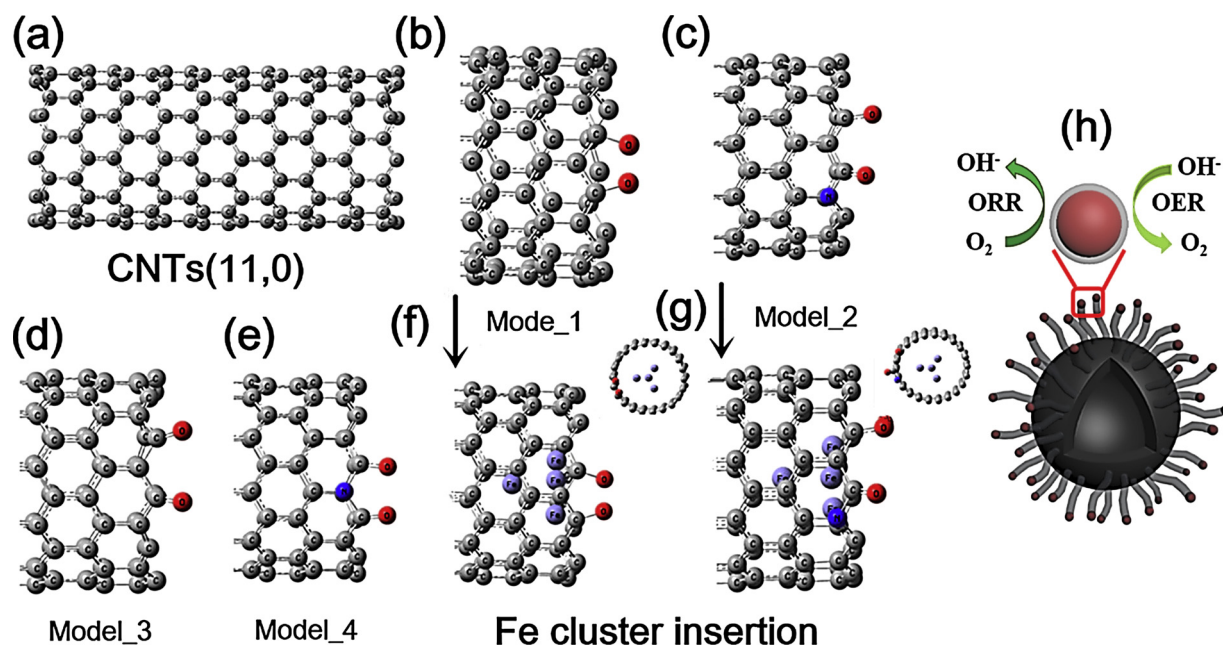


Fig. 6. Obtained structures of PM6 calculations on O₂ adsorption for different models. Schematic model of single-walled CNTs (11, 0) (a). Local structures of O₂ adsorption on CNTs (11, 0) (b, d). Local structures of O₂ adsorption on N-doped CNTs (11, 0) (c, e). Selective structures of O₂ adsorption after Fe₄ cluster insertion (f, g). Schematic for electrochemical energy conversion comprises the oxygen reduction and oxygen evolution reactions (h).

filled as electrolyte. An open circuit voltage of this Zn-air battery was determined to be as high as 1.55 V (Fig. S18a). In Fig. S18b, the rechargeable battery loaded with Fe@N-CNT/HMCS displays the charge and discharge polarization curves, the result indicates that Fe@N-CNT/HMCS as cathode has certain charge-discharge ability. As exemplified in Fig. S18c, the Fe@N-CNT/HMCS shows a larger power density of 102 mW cm⁻², comparable to or even outperform than those of previous literature using carbon catalyst (55 mW cm⁻²) [61] or bimetal oxide carbon-based catalyst (82.3 mW cm⁻²) [62]. The discharge current at the 20 mA cm⁻², displays the specific capacity of the Fe@N-CNT/HMCS assembled Zn-air battery with 671.85 mA h g⁻¹ in Figure S18d, higher than N-GRW [63], nNiFe LDH/3D MPC [64] and NiCo₂S₄/N-CNT [65] the previous papers are listed in Table S8. Furthermore, no obvious potential drop in this Zn-air battery when the battery is galvanostatically discharged at 10 mA cm⁻² for 48 h in Fig. S18e, suggesting its outstanding potential for the cathode in Zn-air battery. Interestingly, the three LEDs can be lightened by two series Fe@N-CNT/HMCS Zn-air battery (inset of in Fig. S18e). The excellent electrochemical activity and long-term stability of the Fe@N-CNT/HMCS catalysts facilitate its practical application in alkaline Zn-air batteries.

3.5. Origin of the enhanced electrocatalytic activity

The excellent electrocatalytic activity of the Me@N-CNT/HMCS catalysts is attributed to the synergistic effect of N doping, metal loading, and rambutan-like electrocatalyst morphology. Firstly, the oxygen reaction activity of Me-HMCS and N-HMCS is better than that of HMCS, which suggests that the transition metal and N are the important active sites [66]. When both metallic element and nitrogen introduce carbon skeleton, the Me@N-CNT/HMCS exhibit enhanced oxygen reaction activity compared to the individual metallic element or nitrogen doping, attribute to the synergistic action between metallic element and nitrogen. In addition, the highest pyridinic-N content (4.04 at %), in Fe@N-CNT/HMCS partly contributes to its highest performance in oxygen catalytic reaction compared to pyridinic N content of 1.39 at % for Co@N-CNT/HMCS and 2.71 at% for Ni@N-CNT/HMCS [67,68]. Secondly, the metal is mainly encapsulated by N-doping carbon nano-shells, promoting the electron transfer from the metal to carbon walls

and decreased local work function on the carbon surface for of OOH* intermediate species formation [69]. Moreover, the O₂ adsorption is a critical part for the oxygen reduction reaction. In order to reach a deep understanding role of metallic element to O₂ adsorption in Fe@N-CNT/HMCS catalysts, a series of models which consist of single-walled CNTs (11, 0) (Fig. 6a, 6b, and 6d), N-doped CNTs (11, 0) (Fig. 6c and 6e), as well as combination of Fe₄ cluster were constructed (Fig. 6f and 6g). The cavity of selected CNTs (11, 0) is enough to accommodate the Fe₄ cluster [70]. In the current work, the semi-empirical PM6 quantum chemistry method was employed based on the consideration of computational time and accuracy [71]. All the calculations were performed by Gaussian 09 program [72]. As shown in Fig. 6b (Model-1) and Fig. 6d (Model-3), two typical O₂ adsorption structures were obtained on the edge of CNTs while there are also two typical O₂ adsorption structures present after N-doping due to different doping sites (Fig. 6c and 6e; Model-2 and Model-4). The O₂ adsorption energies were listed in Table S8. It can be seen that the adsorption energies ranger from -109.5 to -181.7 kcal/mol. For model-1 and model-2, (Fig. 6f and 6g), the Fe₄ cluster is fixed at the center of cavity to estimate the contribution to O₂ adsorption energies. Similar insertion models for model-3 and model-4 have been also calculated, which are omitted in the illustrations for concision. It is interesting to find that all of the O₂ adsorption energies are enhanced after Fe₄ cluster insertion into the cavity of CNTs (Table S9). These quantum calculations directly show that the metallic Fe cluster can promote the O₂ adsorption strength in such a chemical environment. These results suggest that Fe@N-CNT on the carbon spheres surface as the reaction site is more favorable for oxygen adsorption. Thirdly, 3D hollow-mesoporous carbon architectures with large surface areas can prevent the limitations of 1D carbon nanotubes from agglomeration and is beneficial for enhanced mass transport during the electrochemical reaction [8]. In this typical structure, the *in situ* growth of N-CNTs enables a strong interaction with the surface of hollow mesoporous carbon, and then offering tight and stable electrical contact between the active material and the electrically conductive carbon additive. Meanwhile, N-CNTs were utilized to serve as a bridge to electrically connect the 3D carbon sphere throughout the whole electrocatalyst. So 1D/3D hierarchical rambutan-like morphology shows both high ORR and OER performance (Schematic diagram in

Fig. 6h).

4. Conclusion

A novel bi-functional Me@N-CNT/HMCS oxygen electrocatalyst was successfully fabricated via a simple *in-situ* method. This oxygen electrocatalyst exhibits a hierarchical rambutan-like morphology with uniform N-CNTs at the surface of hollow mesoporous carbon sphere interconnected carbonaceous frameworks, which provides high conductivity and structural stability. The durability testing results demonstrate that Me@N-CNT/HMCS is an effective electrocatalyst for ORR with a four-electron pathway and is free from methanol crossover. The Me@N-CNT/HMCS as ORR electrocatalysts shows high catalytic activity and stability, which is comparable performance to that of commercial Pt/C catalysts in certain conditions. Overall, the high electrocatalytic performance of Me@N-CNT/HMCS electrocatalysts can be attributed to the synergetic interaction of abundant N and metal catalytic active sites, high conductivity and rambutan-like morphology. This work provides a new strategy to synthesize rambutan-like Me@N-CNT/HMCS electrocatalysts and opens a new avenue for research on the rational design of the structure and component of highly efficient non-precious electrocatalysts, to replace precious metal catalysts for energy conversion applications.

Conflict of interest

The authors declare no conflict of interest.

Acknowledgments

The authors genuinely appreciate the financial support of this work by the National Nature Science Foundation of China (21776118, 21476097, 21506081). High-tech Research Key laboratory of Zhenjiang (SS2018002). A Project Funded by the Priority Academic Program Development of Jiangsu Higher Education Institutions. A Project Funded by the Priority Academic Program Development of Jiangsu Higher Education Institutions (KYCX18.2274). This study was supported by the high performance computing platform of Jiangsu University.

Appendix A. Supplementary data

Supplementary material related to this article can be found, in the online version, at doi:<https://doi.org/10.1016/j.apcatb.2018.10.013>.

References

- [1] N. Armaroli, V. Balzani, *Angew. Chem. Int. Ed.* 46 (2007) 52–66.
- [2] K. Joya, Y. Joya, K. Ocakoglu, R. van de krol, *Angew. Chem. Int. Ed.* 52 (2013) 10426–10437.
- [3] Y.P. Zhu, C.X. Guo, Y. Zheng, S.Z. Qiao, *Accounts Chem. Res.* 50 (2017) 915–923.
- [4] J. Suntivich, H.A. Gasteiger, N. Yabuuchi, H. Nakanishi, J.B. Goodenough, Y. Shao-Horn, *Nat. Chem.* 3 (2011) 546–550.
- [5] M.K. Debe, *Nature* 486 (2012) 43–51.
- [6] B. Kang, X.Y. Jin, S.M. Oh, S.B. Patil, M.G. Kim, S.H. Kim, S.J. Hwang, *Appl. Catal. B: Environ.* 236 (2018) 107–116.
- [7] C. Wei, Z.X. Feng, G.G. Scherer, J. Barber, Y. Shao-Horn, Z.C.J. Xu, *Adv. Mater.* 29 (2017) 1606800.
- [8] Z.H. Li, M.F. Shao, Q.H. Yang, Y. Tang, M. Wei, D.G. Evans, X. Duan, *Nano Energy* 37 (2017) 98–107.
- [9] J. Ying, G.P. Jiang, Z.P. Cano, Z. Ma, Z.W. Chen, *Appl. Catal. B: Environ.* 236 (2018) 357–367.
- [10] C.C.L. McCrory, S. Jung, I.M. Ferrer, S.M. Chatman, J.C. Peters, T.F. Jaramillo, *J. Am. Chem. Soc.* 137 (2015) 4347–4357.
- [11] B. Hua, Y.F. Sun, M. Li, N. Yan, J. Chen, Y.Q. Zhang, Y.M. Zeng, B.S. Amirkhiz, J.L. Luo, *Chem. Mater.* 29 (2017) 6228–6237.
- [12] M.B. Stevens, C.D.M. Trang, L.J. Enman, J. Deng, S.W. Boettcher, *J. Am. Chem. Soc.* 139 (2017) 11361–11364.
- [13] Q. Li, R. Cao, J. Cho, G. Wu, *Adv. Energy Mater.* 4 (2014) 1301415.
- [14] L. Zhao, X.L. Sui, J.Z. Li, J.J. Zhang, L.M. Zhang, G.S. Huang, Z.B. Wang, *Appl. Catal. B: Environ.* 231 (2018) 224–233.
- [15] H. Tabassum, R.Q. Zou, A. Mahmood, Z.B. Liang, Q.F. Wang, H. Zhang, S. Gao, C. Qu, W.H. Guo, S.J. Guo, *Adv. Mater.* 30 (2018) 1705441.
- [16] Y.Q. Zhang, M. Li, B. Hua, Y. Wang, Y.F. Sun, J.L. Luo, *Appl. Catal. B: Environ.* 236 (2018) 413–419.
- [17] S.B. Yang, X.L. Feng, X.C. Wang, K. Müllen, *Angew. Chem. Int. Ed.* 50 (2011) 5339–5343.
- [18] J.J. Wu, M.F. Rodrigues, R. Vajtai, P.M. Ajayan, *Adv. Mater.* 28 (2016) 6239–6246.
- [19] T. Varga, G. Ballai, L. Vászárheli, H. Haspel, Á. Kukovecz, Z. Kónya, *Appl. Catal. B: Environ.* 237 (2018) 826–834.
- [20] B. Seo, Y.J. Sa, J. Woo, K. Kwon, J. Park, T.J. Shin, H.Y. Jeong, S.H. Joo, *ACS Catal.* 6 (2016) 4347–4355.
- [21] Z.Y. Zhang, Z.R. Yi, J. Wang, X. Tian, P. Xu, G.Q. Shi, S. Wang, *J. Mater. Chem. A* 5 (2017) 17064–17072.
- [22] J.Y. Cheon, T. Kim, Y.M. Choi, H.Y. Jeong, M.G. Kim, Y.J. Sa, J. Kim, Z. Lee, T.H. Yang, K. Kwon, O. Terasaki, G.G. Park, R.R. Adzic, S.H. Joo, *Sci. Rep.* 3 (2013) 2715–2722.
- [23] S. Li, D.Q. Wu, H.W. Liang, J.Z. Wang, X.D. Zhuang, Y.Y. Mai, Y.Z. Su, X.L. Feng, 7 (2014) 3002–3006.
- [24] J. Liang, R.F. Zhou, Xue.M. Chen, Y.H. Tang, S.Z. Qiao, *Adv. Mater.* 26 (2014) 6074–6079.
- [25] J.Y. Cheon, K. Kim, Y.J. Sa, S.H. Sahgong, Y. Hong, J. Woo, S.D. Yim, H.Y. Jeong, Y. Kim, S.H. Joo, *Adv. Energy Mater.* 6 (2016) 1501794.
- [26] Z.Y. Zhang, S.S. Liu, X. Tian, J. Wang, P. Xu, F. Xiao, S. Wang, *ChemSusChem* 5 (2017) 10876–10884.
- [27] R.F. Zhou, S.Z. Qiao, *Chem. Commun.* 51 (2015) 7516–7519.
- [28] B. Seo, Y.J. Sa, J. Woo, K. Kwon, J. Park, T.J. Shin, H.Y. Jeong, S.H. Joo, *ACS Catal.* 6 (2016) 4347–4355.
- [29] J. Woo, Y.J. Sa, J.H. Kim, H.W. Lee, C. Pak, S.H. Joo, *ChemElectroChem* 5 (2018) 1928–1936.
- [30] S.C. Cai, Z.H. Meng, H.L. Tang, Y. Wang, P. Tsiakaras, *Appl. Catal. B: Environ.* 217 (2017) 477–484.
- [31] Y.F. Song, W. Chen, C.C. Zhao, S.G. Li, W. Wei, Y.H. Sun, *Angew. Chem. Int. Ed.* 56 (2017) 10840–10844.
- [32] J.Y. Wang, M. Xu, J.Q. Zhao, H.F. Fang, Q.Z. Huang, W.P. Xiao, T. Li, D.L. Wang, *Appl. Catal. B: Environ.* 237 (2018) 228–236.
- [33] J. Liang, R.F. Zhou, X.M. Chen, Y.H. Tang, S.Z. Qiao, *Adv. Mater.* 26 (2014) 6074–6079.
- [34] G.A. Ferrero, K. Preuss, A. Marinovic, A.B. Jorge, N. Mansor, D.J.L. Brett, A.B. Fuertes, M. Sevilla, M.M. Titirici, *ACS Nano* 10 (2016) 5922–5932.
- [35] C.W. Xu, L.Q. Cheng, P.K. Shen, Y.L. Liu, *Electrochem. Commun.* 9 (2007) 997–1001.
- [36] T. Osako, S. Nagatomo, Y. Tachi, T. Kitagawa, S. Itoh, *Angew. Chem. Int. Ed.* 54 (2015) 4325–4329.
- [37] Z.B. Lei, C. Nikolay, X.S. Zhao, *Energy Environ. Sci.* 4 (2011) 1866–1873.
- [38] C.X. Guo, C.M. Li, *Energy Environ. Sci.* 4 (2011) 4504–4507.
- [39] L.T. Qu, Y. Liu, J.B. Baek, L.M. Dai, *ACS Nano* 4 (2010) 1321–1326.
- [40] K.P. Gong, F. Du, Z.H. Xia, M. Durstock, L.M. Dai, *Science* 323 (2009) 760–764.
- [41] S.H. Ahn, X.W. Yu, A. Manthiram, *Adv. Mater.* 29 (2017) 1606534.
- [42] H.H. Zhong, Y. Luo, S. He, P.G. Tang, D.Q. Li, N. Alonso-Vante, Y.J. Feng, *ACS Appl. Mater. Interfaces* 9 (2017) 2541–2549.
- [43] S.S. Feng, W. Li, Q. Shi, Y.H. Li, J.C. Chen, Y. Ling, A.M. Asiri, D.Y. Zhao, *Chem. Commun.* 50 (2014) 329–331.
- [44] S. Gupta, L. Qiao, S. Zhao, H. Xu, Y. Lin, S.V. Devaguptapu, X.L. Wang, M.T. Swihart, G. Wu, *Adv. Energy Mater.* (2016) 1601198.
- [45] Q. Li, P. Wu, W. Gao, S.G. Ma, G.Q. Zhang, R.G. Cao, J. Cho, H.L. Wang, G. Wu, *Adv. Mater.* 26 (2014) 1378–1386.
- [46] Q. Li, H. Pan, D. Higgins, R. Cao, G. Zhang, H. Lv, K. Wu, J. Cho, G. Wu, *Small* 11 (2015) 1443–1452.
- [47] H.T. Chung, J.H. Won, P. Zelenay, *Nat. Commun.* 4 (2013) 1922–1926.
- [48] J.M. Lee, B.H. Kwon, H.I. Park, H. Kim, M.G. Kim, J.S. Park, E.S. Kim, S. Yoo, D.Y. Jeon, S.O. Kim, *Adv. Mater.* 25 (2013) 2011–2017.
- [49] G. Wu, K.L. More, C.M. Johnston, P. Zelenay, *Science* 332 (2011) 443–447.
- [50] F.J. Maldonado-Hódar, C. Moreno-Castilla, J. Rivera-Utrilla, Y. Hanzawa, Y. Yamada, *Langmuir* 16 (2000) 4367–4373.
- [51] X.Y. Lu, W.L. Yim, B.H. Suryanto, C. Zhao, J. Am. Chem. Soc. 137 (2015) 2901–2907.
- [52] Z.Y. Liu, G.X. Zhang, Z.Y. Lu, X.Y. Jin, Z. Chang, X.M. Sun, *Nano Res.* 6 (2013) 293–301.
- [53] Z.R. Yi, Z.Y. Zhang, S. Wang, G.Q. Shi, J. Mater. Chem. A 5 (2017) 519–523.
- [54] E. Proietti, F. Jaouen, M. Lefevre, N. Larouche, J. Tian, J. Herranz, J.P. Dodelet, *Nat. Commun.* 2 (2011) 1–9.
- [55] J. Bao, X.D. Zhang, B. Fan, J.J. Zhang, M. Zhou, W.L. Yang, X. Hu, H. Wang, B.C. Pan, Y. Xie, *Angew. Chem. Int. Ed.* 54 (2015) 7399–7404.
- [56] M.R. Gao, Y.F. Xu, J. Jiang, Y.R. Zheng, S.H. Yu, J. Am. Chem. Soc. 134 (2012) 2930–2933.
- [57] Z.H. Wen, S.Q. Ci, Y. Hou, J.H. Chen, *Angew. Chem. Int. Ed.* 53 (2014) 6496–6500.
- [58] X. Liu, W. Liu, M. Ko, M. Park, M.G. Kim, P. Oh, S. Chae, S. Park, A. Casimir, G. Wu, *Adv. Funct. Mater.* 25 (2015) 5799–5808.
- [59] Y.Y. Liang, Y.G. Li, H.L. Wang, J.G. Zhou, J. Wang, T. Regier, H.J. Dai, *Nat. Mater.* 10 (2011) 780–786.
- [60] X.T. Han, C. Yu, S. Zhou, C.T. Zhao, H.W. Huang, J. Yang, Z.B. Liu, J.J. Zhao, J.S. Qiu, *Adv. Energy Mater.* 7 (2017) 1602148.
- [61] J. Zhang, Z. Zhao, Z. Xia, L. Dai, *Nat. Nanotechnol.* 10 (2015) 444–452.
- [62] Z.Q. Liu, H. Cheng, N. Li, T.Y. Ma, Y.Z. Su, *Adv. Mater.* 28 (2016) 3777–3784.
- [63] Y.T. Meng, W.Q. Song, H. Huang, Z. Ren, S.Y. Chen, S.L. Suib, J. Am. Chem. Soc. 136 (2014) 11452–11464.

- [64] H.B. Yang, J.W. Miao, S.F. Hung, J.Z. Chen, H.B. Tao, X.Z. Wang, L.P. Zhang, R. Chen, J.J. Gao, H.M. Chen, L.M. Dai, B. Liu, *Sci. Adv.* 2 (2016) e1501122.
- [65] J. Masa, W. Xia, I. Sinev, A. Zhao, Z. Sun, S. Grutzke, *Angew. Chem. Int. Ed.* 53 (2014) 8508–8512.
- [66] Z.Y. Zhang, T.F. Cao, S.S. Liu, X.M. Duan, L.M. Liu, S. Wang, Y.Q. Liu, *Part. Part. Syst. Charact.* 34 (2017) 1600207.
- [67] C.G. Hu, L.M. Dai, *Angew. Chem., Int. Ed.* 55 (2016) 11736–11758.
- [68] H.W. Liang, X.D. Zhuang, S. Brüller, X.L. Feng, K. Müllen, *Nat. Commun.* 5 (2014) 4973–4979.
- [69] M. Beidaghi, C.L. Wang, *Adv. Funct. Mater.* 22 (2012) 4501–4510.
- [70] J.S. Meng, C.J. Niu, L.H. Xu, J.T. Li, X. Liu, X.P. Wang, Y.Z. Wu, X.M. Xu, W.Y. Chen, Q. Li, Z.Z. Zhou, D.Y. Zhao, L.Q. Mai, *J. Am. Chem. Soc.* 139 (2017) 8212–8221.
- [71] C. Bravin, E. Badetti, F.A. Scaramuzzo, G. Licini, C. Zonta, *J. Am. Chem. Soc.* 139 (2017) 6456–6460.
- [72] M.J. Frisch, et al., *Gaussian 09*, Gaussian, Inc., Wallingford, CT, USA, 2009.